Materials & Design 252 (2025) 113778

Contents lists available at ScienceDirect

Materials & Design

journal homepage: www.elsevier.com/locate/matdes

# Scalable phononic metamaterials: Tunable bandgap design and multi-scale experimental validation

Timon Meier [a,1], Vasileios Korakis [a,1], Brian W. Blankenship [a], Haotian Lu [b], Eudokia Kyriakou [c,d], Savvas Papamakarios [c,e], Zacharias Vangelatos [a], M. Erden Yildizdag [f], Gordon Zyla [c], Xiaoxing Xia [g], Xiaoyu Zheng [b], Yoonsoo Rho [a,h], Maria Farsari [c], Costas P. Grigoropoulos [a,*]

[a] Laser Thermal Laboratory, Department of Mechanical Engineering, University of California, Berkeley 94720-1740 CA, USA
[b] Department of Material Science and Engineering, University of California, Berkeley 94720-1740 CA, USA
[c] Institute of Electronic Structure and Laser, Foundation for Research and Technology, Hellas (FORTH-IESL), GR-70013 Heraklion, Crete, Greece
[d] Department of Materials Science and Engineering, University of Crete, Voutes Campus, 71003 Heraklion, Greece
[e] Department of Physics, National and Kapodistrian University of Athens GR-15784 Athens, Greece
[f] Faculty of Naval Architecture and Ocean Engineering, Istanbul Technical University, Istanbul 34469, Turkey
[g] Materials Engineering Division, Lawrence Livermore National Laboratory, Livermore, CA 94550, USA
[h] Faculty Department of Mechanical Engineering, Ulsan National Institute of Science and Technology, Ulsan 44919, Republic of Korea

## ARTICLE INFO

*Keywords:*
Phononic Metamaterials
Band Structure
Tunable Bandgap Design
Tailored Design Framework
Two-Photon Polymerization
Multi-Scale Experimental Validation

## ABSTRACT

Phononic metamaterials offer unprecedented control over wave propagation, making them essential for applications such as vibration isolation, waveguiding, and acoustic filtering. However, achieving scalable and precisely tunable bandgap properties across different length scales remains challenging. This study presents a user-friendly design framework for phononic metamaterials, enabling ultra-wide bandgap tunability ($B/\omega_c$ ratios up to 172 %) across multiple frequency ranges and scales. Using finite element simulations of a Yablonovite-inspired unit cell, we establish a comprehensive parametric design space that illustrates how geometric parameters, such as sphere size and beam diameter, controls bandgap width and frequency. The scalability and robustness of the framework are validated through experimental testing on additively manufactured structures at both macro (10 mm) and micro (80 μm) scales, fabricated using Stereolithography and Two-Photon Polymerization. Transmission loss measurements, conducted with piezoelectric transducers and laser vibrometry, closely match simulations in the kHz and MHz frequency ranges, confirming the reliability and consistency of the bandgap behavior across scales. This work bridges theory and experiments at multiple scales, offering a practical methodology for the rapid design of phononic metamaterials and expanding their potential for diverse applications across a broad range of frequencies.

## 1. Introduction

Phononic metamaterials have garnered significant attention due to their unique ability to control and manipulate acoustic waves, a property that has enabled breakthroughs in vibration damping, sound insulation, and waveguiding applications [1,2]. These materials are defined by bandgaps, frequency ranges where wave propagation is blocked in certain directions, inhibiting the transmission of sound or vibrations [3–5]. Bandgaps are characterized by the absence of phonon-like modes in the $\omega$-$k$ dispersion space, making these materials highly sought after for applications in structural acoustics, telecommunications, and signal processing [6–9]. Initially, bandgaps have been associated primarily with electronic and phononic structures in solid crystals. Advances in material design, however, have demonstrated that bandgaps can be engineered across a range of length scales, from microscopic to macroscopic. Phononic metamaterials exhibit remarkable scalability, enabling their application across a wide range of length scales and frequency domains. At the microscale, they play a crucial role in surface acoustic

---

* Corresponding author.
*E-mail address:* cgrigoro@berkeley.edu (C.P. Grigoropoulos).
[1] These authors contributed equally to this work.

https://doi.org/10.1016/j.matdes.2025.113778
Received 21 January 2025; Received in revised form 23 February 2025; Accepted 26 February 2025

wave (SAW) filters, which are widely used in wireless communication systems to enhance signal selectivity and filtering precision [10,11]. Recent work has also demonstrated their potential in biomedical ultrasound applications, where metamaterial-based designs can enhance acoustic transmission through high-impedance contrast layers, improving the efficiency of ultrasonic imaging and therapeutic applications [12]. At the macroscale, phononic metamaterials have proven effective for vibration isolation, reducing mechanical noise and structural vibrations in precision engineering and aerospace applications [13–16]. Additionally, they are widely utilized for noise reduction and sound absorption in architectural acoustics, automotive sound insulation, and industrial environments, where their tailored bandgaps help mitigate unwanted noise [17–21]. Advances in 3D printing and nanofabrication have further expanded their potential, enabling the development of broadband metamaterial absorbers and high-performance acoustic wave manipulation devices [22,23]. These capabilities make phononic metamaterials a promising platform for next-generation acoustic technologies, spanning from high-frequency medical applications to large-scale structural noise control.

The formation of bandgaps in phononic metamaterials fundamentally relies on the periodicity of their structural design [24]. Periodicity alters the governing wave equation, allowing transformations into Fourier space, where dispersion relations for each phonon mode are derived. Bandgaps arise through mechanisms like Bragg scattering [25] and resonant modes [26] depending on the geometric configuration and material properties of the unit cells [27–29]. These mechanisms enable to block wave transmission within bandgap frequencies, thus providing robust control over vibration propagation. In early phononic metamaterial designs, researchers primarily used simple 2D geometries, such as rods or holes. These designs were constrained by the scalar acoustic wave equation, which describes pressure waves with a single degree of freedom [24,30]. The advent of elastic bandgap metamaterials introduced designs governed by the full elastic wave equation, allowing for three degrees of freedom in each direction. This development enabled the manipulation of both transverse and longitudinal waves, supporting the creation of customized bandgaps for specific wave modes, including bending, tensile, and shear waves [31]. Moreover, the introduction of anisotropic and auxetic metamaterials has allowed for selective bandgap formation by contrasting auxetic, non-auxetic and directional properties, highlighting the versatility of phononic metamaterials [32–35].

Modern computational tools, particularly finite element analysis (FEA), have revolutionized the design of phononic metamaterials, allowing for precise simulation of wave propagation and bandgap prediction. Dynamic tunability has further expanded the operational range of these materials through reconfigurable geometries, local resonators, and inertial amplification techniques, which enhance their elastodynamic properties [7,31]. However, while these methods have been successfully implemented at larger scales and lower frequencies, extending their functionality to the microscale and high-frequency regimes (hundreds of kilohertz to megahertz) remains a challenge due to fabrication and scalability constraints [36]. These limitations restrict their application in high-frequency domains, such as medical ultrasound [12], high-resolution imaging systems, non-destructive testing, and compact acoustic signal processing devices, where precise wave control is critical [37–39].

To overcome these challenges, advancements in additive manufacturing methods have emerged as transformative solutions, enabling the realization of complex μm-scaled metamaterials with unprecedented precision. Techniques such as Two-Photon Polymerization (2PP) and Digital Light Processing (DLP) offer high resolution and scalability, allowing for complex geometries suited for high-frequency phononic applications. 2PP, with its sub-micron resolution, has proven particularly effective for creating complex 3D geometries suitable for high-frequency phononic applications, making it an indispensable tool for scaling designs [40–42]. Alongside these fabrication techniques, recent diagnostic advancements, such as laser vibrometry and laser-induced spectroscopy, have further facilitated the experimental characterization of wave propagation at the microscale, bridging the gap between numerical predictions and real-world performance [39,43,44]. Transmission loss measurements and laser vibrometry analyses have confirmed the presence of elastodynamic bandgaps, demonstrating the reliability of these advanced fabrication and characterization methodologies [9,45–48].

The design of phononic metamaterials often requires extensive parametric optimization of unit cells, with existing methods broadly categorized into direct parameter tuning and computational optimization. Traditional direct tuning approaches rely on prior knowledge of bandgap formation mechanisms, such as Bragg scattering and local resonances, systematically adjusting structural parameters to generate bandgap maps. For example, Muhammad et al. [13] proposed monolithic phononic metastructures that achieved ultrawide bandgaps of up to 160 % for low-frequency vibration isolation in the kHz range, validated experimentally using laser vibrometry. Similarly, Li et al. [29] utilized Hoberman spherical metamaterials optimized for local resonances, achieving broad bandgap coverage specifically in low-frequency regimes. An et al. explored geometric reconfigurations to achieve tunability, such as adjusting the spacing between inclusions or altering chiral lattice angles, resulting in variable bandgap distributions [15]. Additionally, other research efforts have proposed and experimentally validated 2PP metamaterials that demonstrate unique functionalities, such as ultra-wide bandgaps in the MHz range [48] or serving as phonon polarizers for specific applications [39]. Further approaches have leveraged the coexistence of Bragg scattering and local resonances to achieve tunable bandgaps. For instance, Jia et al. [49] demonstrated that hexagonal structures can achieve bandgap widths reaching up to 100 % in the kHz range by carefully combining these two mechanisms. Similarly, Olsson et al. [50] designed phononic crystals by precisely matching Bragg and Mie scattering inclusions within silicon-based substrates, achieving an average bandgap width of 46 % in the MHz range. Other work has explored geometric reconfigurations for tunability, where the spacing between square inclusions was adjusted through rotational transformations, resulting in tunable bandgaps ranging from 0 % to 80 % [51]. Auxetic metamaterials incorporating high-density inclusions have also been developed to modify the Poisson's ratio of unit cells, achieving bandgap widths of up to 30 % [52–54]. While these methods have proven effective in various scenarios, they often require extensive trial-and-error processes, are limited in scalability, or only cover specific frequency ranges, thereby limiting their practical application in a broader range of high-frequency technologies.

To address these limitations, modern computational optimization frameworks have emerged, allowing for automated bandgap tuning. Among these approaches, topology optimization has been widely employed to maximize bandgap width and minimize transmission loss [55,56]. For instance, Zhang et al. [56] used genetic algorithms to iteratively widen the bandgap regions of multifunctional metamaterials, achieving tunable bandgaps up to 60 %. Other advanced methods integrate parametric maps with resonance effects to achieve bandgap control over a broad frequency spectrum, with experimental validation at the microscale [43]. Additionally, genetic algorithms have been widely employed to refine bandgap properties [57], while topology optimization strategies have successfully minimized transmission loss and expanded bandwidths [58,59]. Recent research has introduced classification-based methods that categorize unit cells based on complexity to refine bandgap engineering. Additionally, artificial intelligence-driven inverse design techniques, such as generative and reinforcement learning, have been developed to achieve more precise and automated designs [60–63]. While these computational methods offer greater design flexibility, they remain highly resource-intensive, requiring significant computing power and often resulting in intricate geometries that are challenging to fabricate, thereby limiting their feasibility for practical applications.

In contrast, our framework provides a scalable, computationally efficient, and experimentally validated alternative by eliminating the need for iterative inverse design and complex topology optimization. Rather than relying on predefined physical heuristics or computationally expensive inverse design techniques, we establish a precomputed parametric design space using a non-dimensionalized scaling law, making it inherently adaptable across different length scales and frequency regimes. Unlike previous methods that require extensive computation for each new unit cell design, our approach enables rapid bandgap tuning by adjusting geometric scaling parameters independent of the specific unit cell configuration.

Our methodology is built upon FEA simulations of a Yablonovite-inspired cubic unit cell [64], selected for its inherent symmetry and compatibility with diverse manufacturing methods. By incorporating spherical mass elements, we fine-tune bandgap frequencies, creating a versatile design space adaptable to different frequency ranges and scales. Central to this study is the development of a non-dimensionalized scaling law that generalizes bandgap design across orders of magnitude in unit cell size. With the established design space, bandgap properties can be easily tailored by adjusting geometrical scaling parameters.

A key differentiator of our work is the experimental validation of bandgap tunability across multiple length scales. To demonstrate the robustness and scalability of our approach, we fabricate optimized designs at both the millimeter scale (10 mm) using Stereolithography (SLA) and the microscale (80 μm) with a custom-built 2PP setup. Experimental validation through piezo actuation and laser vibrometry transmission loss measurements confirm not only the feasibility of our framework but also its ability to maintain consistent performance across orders of magnitude in unit cell size. Moreover, our approach offers a broader range of tunability, encompassing most previous designs at various scales, covering frequency ranges from kHz to MHz. The ability to systematically scale phononic metamaterials while preserving bandgap characteristics is crucial for applications in vibration isolation, acoustic waveguiding, and ultrasound technologies. While GHz-range nanoscale phononic materials [65] remain an area of interest, their development is currently constrained by fabrication and measurement limitations. However, our parametric design framework lays a foundation for potential extensions to nanoscale phononic metamaterials, contingent on future advancements in manufacturing and characterization techniques.

## 2. Materials and methods

### 2.1. Unit cell selection

The initial unit cell configuration for this study is based on a Yablonovite structure [64,47] characterized by rods capped with spheres arranged in a simple cubic lattice. This design was selected after a detailed exploration of several configurations and offers multiple advantages:

First, the simple cubic arrangement enhances the symmetry of the unit cell, which simplifies the interpretation of results and facilitates the design process by providing a straightforward *k*-path in the Brillouin zone to calculate bandgap properties. This symmetry allows for efficient computation of dispersion relations and ensures predictable phononic behavior. Second, the selected unit cell design offers scalability and adaptability across different manufacturing techniques, such as SLA and 2PP, allowing for experimental validation at micro and millimeter scales without compromising performance. Lastly, the unit cell's bandgap properties can be easily tuned by modifying parameters such as beam thickness ($D_B$) and sphere diameter ($D_S$) [43,66], making it versatile for various acoustic, ultrasonic and mechanical applications, enabling precise design adjustments based on specific requirements.

To determine the most effective unit cell design for our framework, we systematically evaluated multiple mass-beam configurations, including center mass, corner mass, and edge mass designs. Our analysis, shown in Supplementary Information (SI) Fig. S4, revealed that the center mass configuration exhibited a significantly smaller bandgap range with poor tunability, whereas both the corner mass and edge mass configurations provided broader, more tunable bandgap properties. Based on these findings, we selected the edge mass configuration as the basis for our design framework to streamline the process and provide a simplified, yet comprehensive, user-friendly design space. Beyond these configurations, we investigated other well-known beam architectures, including octet trusses, face-centered designs, and body-centered designs, commonly studied in mechanical metamaterials [67,68]. However, simulations confirmed that these geometries did not exhibit phononic bandgaps in the frequency ranges of interest, making them unsuitable for our objectives. Furthermore, we prioritized simpler geometries over highly intricate designs to ensure scalability and manufacturability across different length scales. Pursuing overly complex geometries would contradict our focus on practical applicability and user accessibility.

Fig. 1 presents an overview of our study, illustrating the design, simulation, and validation process, from initial FEA simulations and predictive modeling (A) to fabrication at two distinct scales and experimental validation (B).

### 2.2. Bloch-wave analysis and Transmission loss simulation

We conducted simulations in COMSOL Multiphysics 6.0, using the Solid Mechanics module for frequency domain analysis. Alternative ray models exist in the literature [69] but we chose the solid mechanics equation analysis to exclude errors introduced by such approximations. Bloch-wave analysis within the finite element framework provided the dispersion relation and a numerical measure of longitudinal rod-wave velocity for all lattice designs. Due to the symmetry of the braced-cubic unit cell, we used a cubic symmetric irreducible Brillouin Zone [70]. To enable exploration of phonon-like solutions, Bloch-Floquet periodic boundary conditions were applied. The structure was meshed with quadratic tetrahedral elements, ensuring at least four divisions across each strut's thickness for accuracy. For the bandgap diagrams, we assigned material properties specific to the SLA macrostructure and 2PP microstructure, as detailed in the fabrication section. To isolate bandgaps that arise from the geometry alone, we assumed the unit cell was not immersed in a liquid medium, thereby avoiding potential acoustic impedance mismatches. An infinite impedance mismatch was imposed between air and polymer, effectively excluding air from the calculations [71].

For the transmission loss simulations, we modeled the fabricated, finite 5 × 5 × 5 structures. The solid mechanics solver computed velocity at the top plate in response to a unit displacement applied at the bottom plate. Transmission loss was calculated over a range of frequencies, with the wave transmission curve along the excitation direction, measured in decibels (dB), calculated as:

$$TL = 20\log_{10}\mathrm{avg}(u_{top})$$

### 2.3. Fabrication

Macroscale samples were fabricated using digital light processing (DLP) 3D printing technology with Anycubic Photon D2 printer (ANYCUBIC Technology Co., Ltd). The materials employed for the SLA macrostructure included ANYCUBIC DLP Craftsman resin, chosen for their high precision. Printing parameters were set as recommended by the manufacturer on their website (Layer thickness: 0.05 mm, Exposure time: 2.5 s, Light-off time: 1 s, Z lift distance: 5 mm, Z lift speed: 3 mm/s). Density, Youngs modulus and Poisson ratio of the base material were found to be: $\rho = 1.1$ g/cm$^3$, $E = 1100$ MPa, $\nu = 0.49$. SLA fabrication offers a broader range of material choices, typically photopolymers, which are cost-effective and sufficiently stiff for experimental validation.

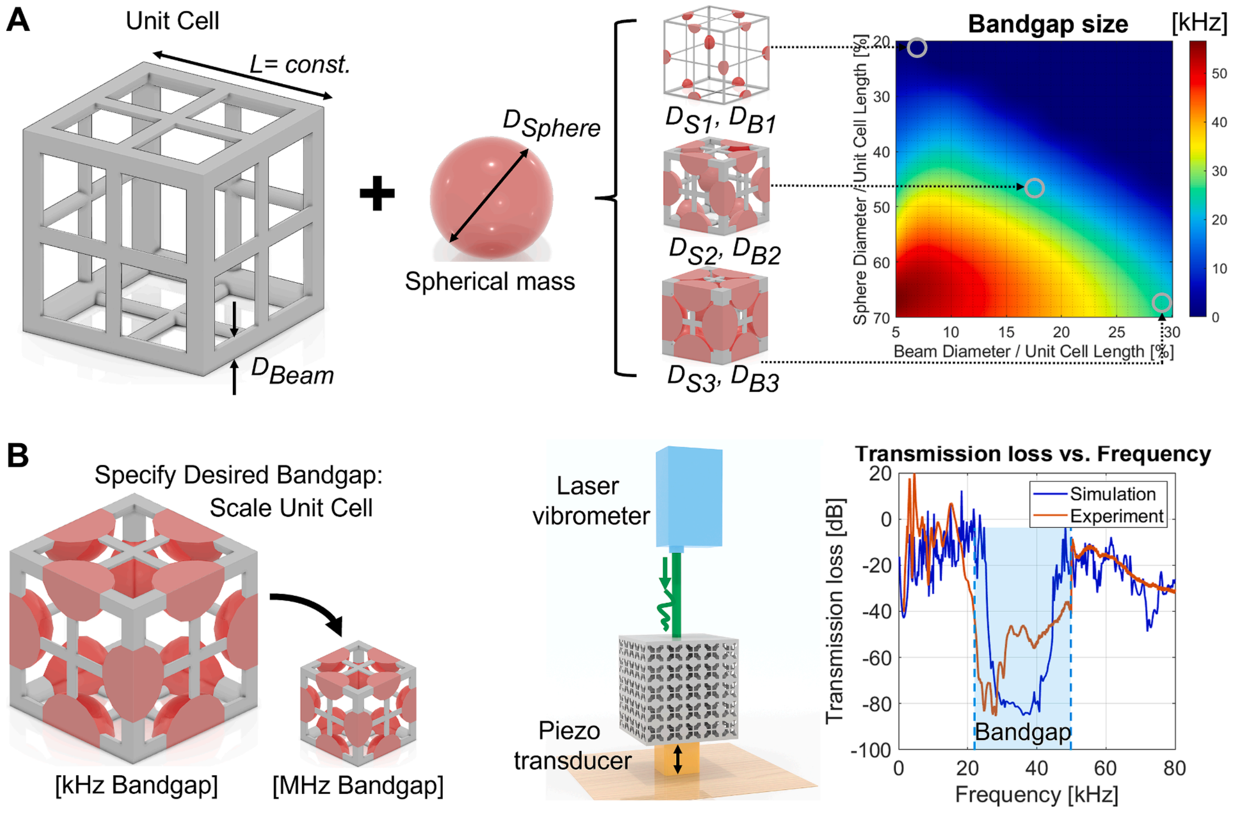

**Fig. 1. Framework for the design and validation of scalable phononic bandgap metamaterials.** A) Schematic of a parametrized Yablonovite-inspired unit cell featuring spherical masses connected by struts, with tunable geometric parameters. FEA simulations explore various parametric $D_S$, $D_B$ combinations, mapping the design space for achieving phononic bandgaps. B) Predictive unit cell design. Users specify desired bandgap properties, such as frequency range and width, which can simply be achieved by scaling the unit cell parameters. We demonstrate this scaling in two distinct scales and provide experimental validation of bandgap properties in macro and micro scale conducted using piezoelectric transducers and laser vibrometry transmission loss measurements.

The microlattice structures were fabricated using a polymer resin (IP-DIP Photoresin, Nanoscribe) with a density of $\rho = 1.2\ \mathrm{g/cm^3}$, well-suited for 2PP. 2PP is limited to a smaller selection of resins optimized for two-photon absorption. Furthermore, fabrication time increases significantly for large or intricate structures, making multi-unit cell arrays more challenging to produce at high throughput. Fabrication was carried out using a custom-built 2PP system. This system employs a tightly focused, near-infrared femtosecond laser beam (InSight® X3+, Spectra-Physics) with a peak wavelength of approximately 800 nm, a pulse width of 100 fs, and an 80 MHz repetition rate. The beam is focused within the resin using an oil immersion 25X objective lens (NA 0.8, Carl Zeiss) to achieve a voxel resolution with lateral dimensions of 500 nm and an axial resolution of 3.46 μm under Abbe diffraction limit conditions. The high photon flux (~1 TW/cm2) generated by the femtosecond pulses induced localized cross-linking of the polymer resin, facilitating precise structure formation through the 2PP process. A two-axis galvanometer mirror scanner (Excelliscan 14, ScanLAB) directs the laser laterally at a scan speed of 100 mm/s with 0.25 μm hatching, while a linear z-stage adjusts the vertical positioning in 1 μm increments between layers. Post-fabrication, the printed structures are immersed in a propylene glycol monomethyl ether acetate (PGMEA) bath for 1 h to dissolve any unpolymerized resin. This is followed by a 1-hour rinse in isopropanol to remove residual solvent, leaving a clean, stable microlattice structure ready for experimental analysis. Under these printing conditions the Young's modulus of the base resin was found to be $E = 1400$ MPa.

### 2.4. Wave transmission experiments

To experimentally validate the theoretical dispersion and transmission loss simulations, we conducted vibration experiments using 5 × 5 × 5 arrays of the phononic metamaterial, each with thin covering plates on the top and bottom.

For the SLA macroscale structures, the bottom plate was secured to a piezoelectric transducer (Thorlabs, Item: PC4QM) with a clear epoxy to minimize damping effects. The top plate served as the measurement plane for the laser scanning vibrometer (Polytec GmbH, PSV-500). During testing, a sinusoidal wave frequency sweep was applied ranging from 1–90 kHz over a 64-second sweep time, with an amplitude voltage of 10 V and a sampling frequency of 215 kHz.

For the 2PP-fabricated microscale structure, the bottom plate was attached to a different piezoelectric transducer (APC International, LTD, Item: 70–3000) using an epoxy. The top plate again served as the measurement plane for the laser vibrometer. Frequency sweeps for this structure covered 0.5 to 8 MHz, with a sweep time of 64 s, an amplitude voltage of 10 V, and a sampling frequency of 16 MHz.

To ensure adequate vibration absorption, we utilized five-unit cells per dimension, as vibrations are attenuated exponentially per cell within the designated bandgap. The laser vibrometer is used to measure the velocity spectrum of a vibrating point. First, the vibrometer captured baseline velocity data of the piezoelectric surface $v_i$ and then velocity data of the sample with the structure affixed on top $v_s$. The resulting spectrum was plotted on a logarithmic scale to illustrate the transmission losses, calculated using the formula:

$$TL = 20\log_{10}\left(\frac{v_s}{v_i}\right)$$

A detailed schematic and a photograph of the experimental setup have been included in the SI (Fig. S7a, S7b). Laser focusing and calibration were conducted prior to each measurement to ensure precise and repeatable data acquisition. Given the small unit cell size in microscale samples, careful laser spot alignment was necessary to ensure the vibrometer's focal point accurately targeted the structure, minimizing potential measurement artifacts.

To obtain accurate frequency-dependent transmission loss, FFT analysis was applied to the raw velocity data, converting the time-domain signal into the frequency domain. The resulting transmission loss spectrum quantified the attenuation of wave amplitude, serving as a direct experimental validation of the phononic bandgap behavior.

## 3. Results

### 3.1. Design framework

The dispersion relation $\omega = \omega(k)$ represents a set of curves (modes) describing vibration propagation in a unit cell. In the $(\omega, k)$ graph, regions devoid of modes, known as bandgaps, signify frequencies where wave propagation is inhibited. A bandgap is characterized by its frequency width, $B = \omega_u - \omega_l$, where $\omega_u$ and $\omega_l$ are the upper and lower frequency bound of the bandgap, and its center frequency $\omega_c = (\omega_u + \omega_l)/2$. The primary design objective is to engineer unit cells with specific bandgap widths and positions to effectively eliminate undesirable vibrations within targeted frequency ranges. To achieve this, we utilized FEA in COMSOL Multiphysics to calculate dispersion curves for a cubic-symmetric, Yablonovite-inspired unit cell (Fig. 2a) under the assumption of infinite periodicity in all directions. Our design framework introduces tunability through the addition of spherical masses of varying diameters within the lattice, as well as adjustments to strut dimensions. These modifications enable scalable and manufacturable metamaterial designs applicable across multiple length scales.

Fig. 2b presents the simulated dispersion diagram for a unit cell, featuring the parameters $L = 10$ mm, $D_B = 1.875$ mm, and $D_S = 5$ mm. Along the irreducible Brillouin zone path for cubic-symmetric structures (*Γ-X-M-Γ-R-X-M-R*) [70], the structure exhibits a first bandgap centered at $\omega_c = 35$ kHz, with upper and lower bounds $\omega_u = 47$ kHz and $\omega_l = 23$ kHz.

The bandgap formation mechanism is primarily driven by resonance, as indicated by the agreement between the simulated modes (Fig. 2b) and classical phonon dispersion solutions [72] along $k = \Gamma \rightarrow X$. Previous studies have attempted to model the bandgap formation mechanism using a similar approach, as seen in [73,74]. A concise explanation of this mechanism is provided in the SI (Fig. S1-S3). The analytical framework for phonon propagation serves as the foundation for deriving the dispersion relation presented in Eq. (1).

$$\omega^2 = A + \sum_{i=1}^{i=4} \alpha_i \cos(i\pi k), \qquad k \in (-1, 1) \tag{1}$$

where $A$ and $\alpha_i$ are fitting coefficients. Notably, the first bandgap spans the entire $k$-space, effectively blocking oscillations in all directions and serving as the primary absorber for undesirable vibrations. To generalize the design across scales, the dispersion relation $\omega = \omega(k)$ is non-dimensionalized as (Eq (2)., [75]):

$$\widehat{\omega} = \omega \frac{L}{c}, \qquad \widehat{k} = kL \tag{2}$$

where $L$ is the size of the unit cell, and $c$ represents the speed of sound for transverse or longitudinal waves. This scaling law predicts bandgap properties for different frequency ranges by varying the unit cell dimensions. For example, a unit cell size $L'$ scales the bandgap position and width as follows (Eq. (3):

$$B' = B\frac{L}{L'}, \qquad \omega_c' = \omega_c \frac{L}{L'} \tag{3}$$

Thus, bandgap position inversely scales with unit cell size, offering precise tunability for different frequency ranges. To tailor and optimize bandgap characteristics, we performed parametric simulations by systematically varying the sphere and beam diameter to length ratios ($D_S/L$ and $D_B/L$) while maintaining constant material properties, such as Young's modulus and Poisson's ratio.

Fig. 3a displays a resulting colormap of the Bandgap size ($B$) to bandgap center frequency ($\omega_c$) ratios across these parameter combinations, with $L = 10$ mm. To further enhance user accessibility, Fig. 3b and 3c illustrate how bandgap center frequency ($\omega_c$) and bandgap width ($B$) vary independently across the same parameter space. Increasing sphere diameter increases mass, which widens the bandgap, whereas larger

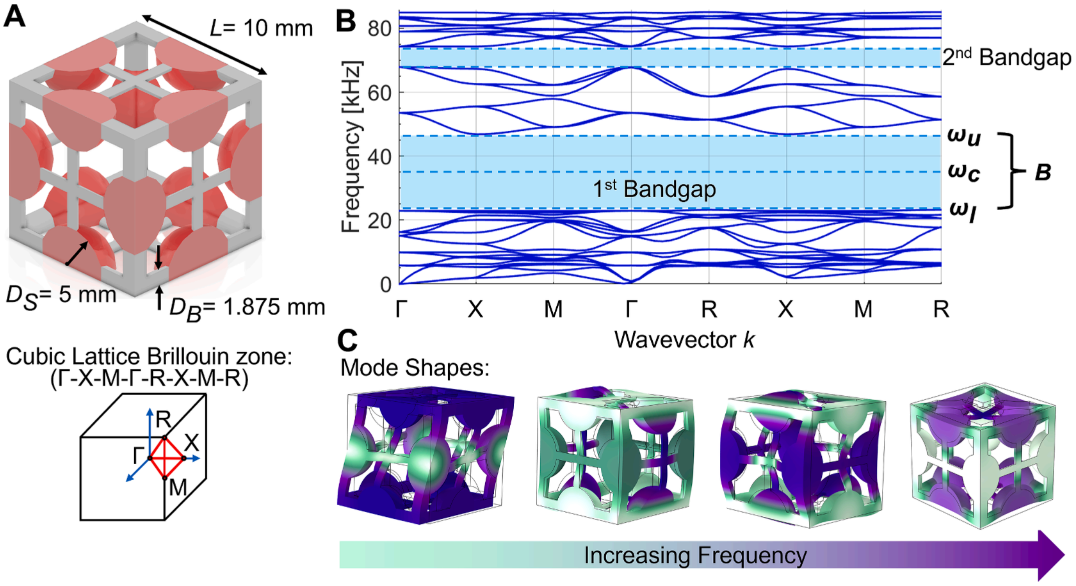

**Fig. 2. Illustration of the Yablonovite-inspired unit cell structure and its phononic bandgap behavior.** A) Schematic of the unit cell structure featuring tunable parameters: lattice constant $L = 10$ mm, beam diameter $D_B = 1.875$ mm, and sphere diameter $D_S = 5$ mm, as utilized in FEA simulations. B) Corresponding simulated bandgap diagram along the Brillouin zone path (*Γ-X-M-Γ-R-X-M−R*), showing a bandgap centered at$\omega_c = 35$ kHz with bounds$\omega_u = 47$ kHz and$\omega_l = 23$ kHz. The dispersion relation $\omega = \omega(k)$ highlights the frequency ranges (bandgaps) where no vibrational modes are present, effectively blocking wave propagation in this range. C) Mode shapes corresponding to increasing frequency, illustrating the physical deformation patterns within the unit cell at selected points across the spectrum.

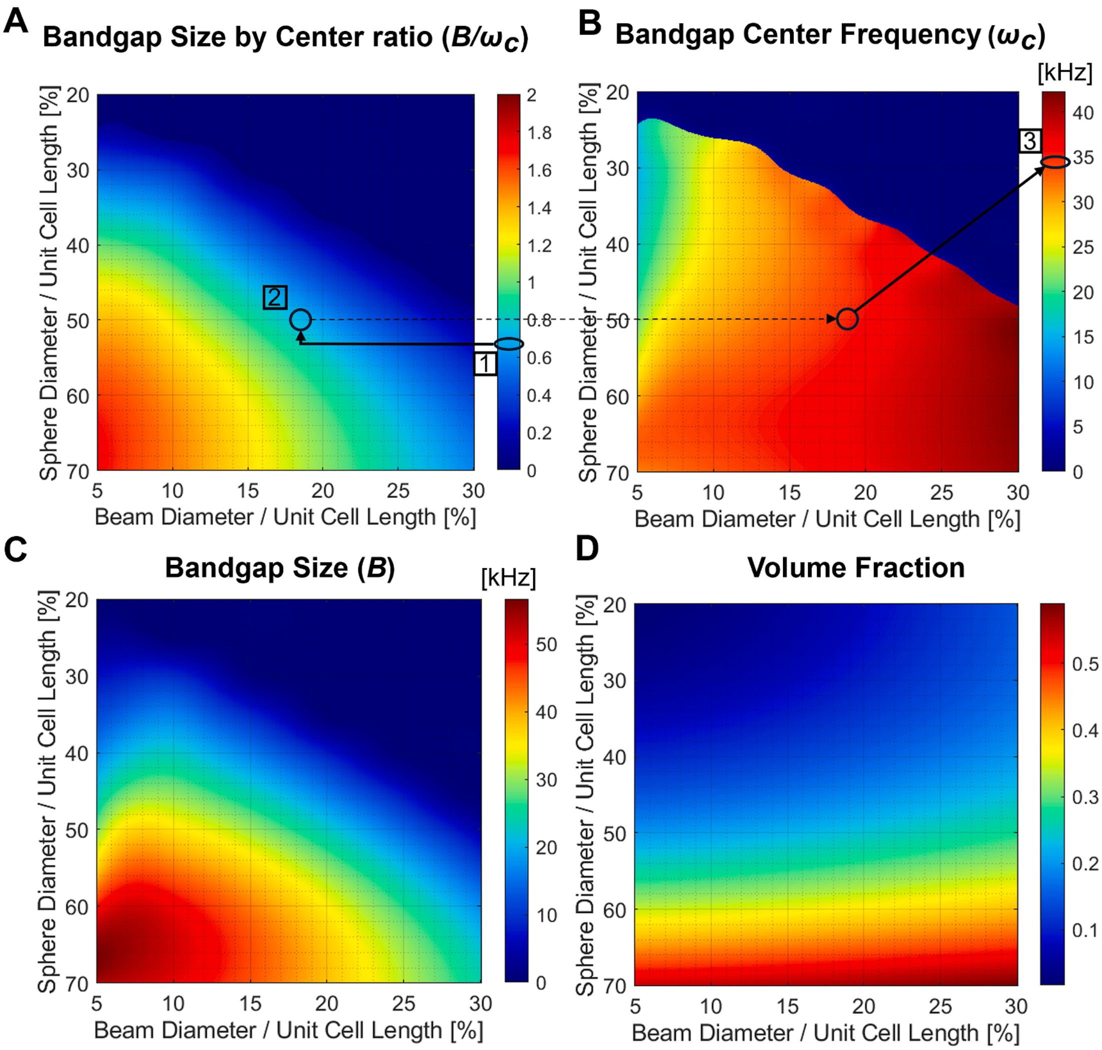

**Fig. 3. Colormaps illustrating the effects of varying design parameters on bandgap size and characteristics in the unit cell design space.** A) Colormap displaying the normalized ratio of bandgap size to center frequency ($B/\omega_c$) as a function of different sphere-to-length ($D_S/L$) and beam-to-length ($D_B/L$) ratios for a unit cell with $L = 10$ mm. The design space spans $B/\omega_c$ ratios from 0 to 1.72, offering a wide range of tunable bandgap behaviors. B) and C) Colormaps showing how the bandgap center frequency $\omega_c$ and bandgap size $B$ vary individually across the parameter space. Increasing sphere diameter widens the bandgap, while larger beam diameter narrows the bandgap and increases $\omega_c$. D) Colormap depicting the volume fraction of parameterized geometries, illustrating the relationship between geometric scaling and phononic bandgap properties. Visual annotations and comments guide users through the four-step process of tailoring specific bandgap characteristics: (1) Calculate desired $B'/\omega'_c$ ratio, (2) selecting a matching $D_S/L$, $D_B/L$ design point, (3) retrieving $\omega_c$ for chosen design, and (4) scaling the unit cell length ($L = 10$ mm) by the $\omega_c/\omega'_c$ ratio to match the desired operating frequency. This framework enables rapid design customization for targeted applications, highlighting the interplay between geometric scaling and phononic bandgap properties.

strut diameters shift to higher frequencies while reducing bandgap width. Additionally, Fig. 3d shows the volume fraction of different parameterized geometries. Volume fraction is a key metric in architected materials, influencing both mechanical performance and manufacturability. These colormaps provide a comprehensive understanding of how geometric variations impact both structural mass distribution and phononic characteristics.

The design space parameters, limited by structural stability and manufacturability, support bandgaps with $B/\omega_c$ ratios from 0 to 1.72. At low $B/\omega_c$ ratios, adjacent modes in the dispersion relation can overlap or have insufficient separation, reducing the ability to form distinct bandgaps. This occurs when the contrast between stiffness and mass is too small, limiting Bragg scattering and local resonance effects. At high $B/\omega_c$ ratios, structural stability and manufacturability become limiting factors. Large $B/\omega_c$ values often require thin struts and large masses, which can lead to mechanical instability, such as buckling or deformation. For instance, unit cells with the highest $B/\omega_c$ ratios in our design space feature large spherical masses and thin connecting struts, making them highly susceptible to structural failure under external loading.

The colormaps in Fig. 3 enable users to design bandgaps with tailored widths and positions, guided by a straightforward scaling law. The process starts by defining a target bandgap size $B'$ and center frequency $\omega'_c$. For example, if the target frequencies are $B'$= 3.0 MHz and $\omega'_c$ = 4.375MHz, frequencies suitable for biomedical ultrasound applications or for wireless communication in the HF region [12,76], we calculate the ratio $B'/\omega'_c = 0.69$. This ratio is then used to locate corresponding design points on the colormap (Fig. 3a). Since multiple parameter combinations can yield the same ratio, additional factors like mechanical strength or size constraints can guide the final selection. Once a design point is chosen, the associated center frequency is retrieved from Fig. 3b. For this example, the selected parameters $D_s/L =$ 0.5 and $D_B/L = 0.1875$, correspond to a center frequency of $\omega_c = 35$ kHz for a standard unit cell size of $L = 10$ mm. Using the scaling law to align with the desired frequency, the unit cell length is adjusted: $\omega_c/\omega'_c = \frac{35\mathrm{kHz}}{4.375\mathrm{MHz}} = \frac{1}{125}$, yielding a scaled unit cell length of $L' = 1/125 \cdot 10$ mm =

80 μm. Simulations (Fig. S6) confirm that this final design retains its target bandgap properties. This framework allows for the effortless customization of bandgaps to meet specific frequency requirements, bypassing the need for additional simulation or optimization.

### *3.2. Properties of fabricated samples*

To validate the theoretical and simulation results, we fabricated two sets of samples using two distinct fabrication techniques: SLA for the larger structures (10 mm unit cell size) and 2PP for the microscale structures (80 μm unit cell size). These methods were chosen for their precision and ability to replicate the complex geometries required at both scales. Bandgap formation is influenced not only by geometric parameters but also by material properties such as Young's modulus. Due to differences in material stiffness, additional simulations were conducted to account for the 25 % higher Young's modulus of the 2PP polymer compared to the SLA resin, which was evaluated through compression experiments. This variation directly influences the predicted bandgap properties, as an increase in Young's modulus results in a proportional shift in the bandgap center frequency, as demonstrated in SI Fig. S6. For the fabricated 2PP structure with parameters $L = 80$ μm, $D_s/L = 0.5$ ($D_s = 40$ μm) and $D_B/L = 0.1875$ ($D_B = 15$ μm) the adjusted bandgap width and center frequency are predicted as $B' = 3.2$ MHz and $\omega'_c = 5.4$ MHz.

For experimental testing, we fabricated sample arrays with a 5 × 5 × 5 unit cell configuration to balance fabrication time and performance. While simulations assume infinite periodicity, the finite size of the fabricated sample arrays (5 × 5 × 5 unit cells) was sufficient to approximate bulk material behavior. Wave interactions and bandgap effects were observed to stabilize after a sufficient number of repeated unit cells, with minimal edge effects. These edge effects had a negligible impact on the dominant wave propagation within the interior of the material, confirming that the sample size was large enough to maintain the accuracy of the bandgap performance for the bulk material. This choice of sample size is supported by previous work, where longitudinal and transverse bands for tessellations with $> 5$ repeating unit cells were found to be in agreement within the long-wavelength limit [39,44].

Images of the SLA and 2PP samples are presented in Fig. 4, with additional SEM images included in SI (Fig. S8) to provide further insights into the fabricated structures. Visual inspection confirmed the geometric accuracy of the fabricated unit cells, with all samples maintaining the intended design parameters derived from the parametric simulations. Additionally, the structures exhibited no significant deformation or defects. This confirms the fidelity of the fabrication process and supports the validity of the scaling law across different size scales and material properties. The images also highlight the high surface quality of the top surfaces, which provides a stable and reliable foundation for laser vibrometer measurements. Smooth surfaces can reduce measurement noise and improve the accuracy of velocity data acquisition during transmission loss experiments.

### *3.3. Experimental analysis*

Theoretical bandgap properties of phononic metamaterials are often derived from dispersion diagrams, however dispersion curves $\omega(k)$ are challenging to measure experimentally, particularly for complex three-dimensional structures. Dispersion diagrams provide critical insight into wave propagation and bandgap formation but require sophisticated equipment and complex procedures, such as scattering experiment [77,65,44], to directly measure the $\omega$-$k$ relation. Given these practical limitations, transmission loss measurements serve as a more accessible and effective method for experimental validation. Transmission loss quantifies the attenuation of wave amplitude as vibrations pass through a structure, offering a direct indicator of bandgap behavior. Within a

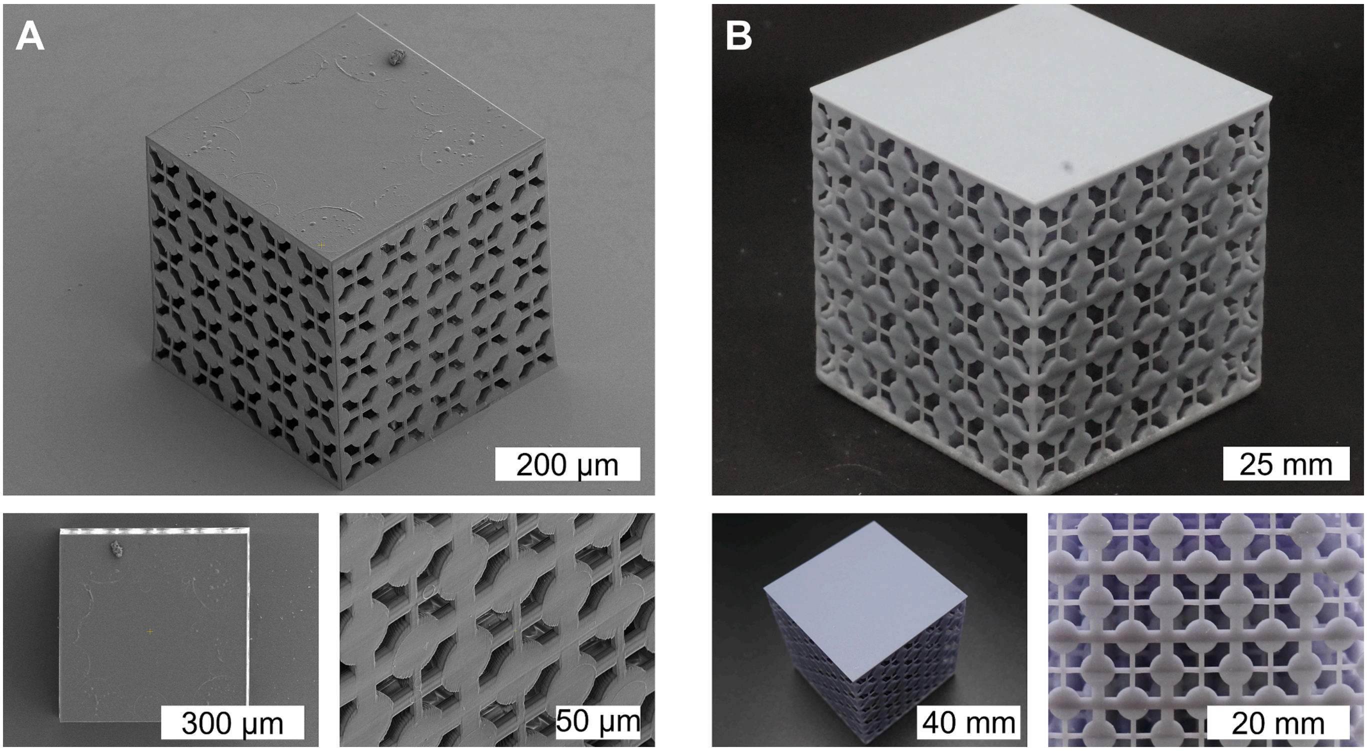

**Fig. 4. Fabricated phononic metamaterials at micro- and macro-scales.** A) Scanning electron microscope (SEM) images of a 5 × 5 × 5 array of unit cells fabricated using 2PP. The unit cell size is 80 μm, with detailed views highlighting the high-resolution features and precision of the microstructured lattice. Isometric, top-down, and close-up views demonstrate the fidelity of the fabrication process. B) Isometric and close-up views of a 5 × 5 × 5 array of unit cells fabricated using SLA. The unit cell size is 10 mm, representing the macroscale counterpart. This dual-scale fabrication demonstrates the versatility of the design framework, enabling the realization of phononic metamaterials across a wide range of scales for diverse applications.

bandgap, the structure significantly attenuates wave propagation, resulting in higher transmission loss. This indirect approach reliably correlates with the bandgap regions predicted by dispersion simulations.

To simulate the transmission loss, we used the solid mechanics module in COMSOL Multiphysics. A sinusoidal input displacement ($u_{in}$) was applied to the bottom surface of the $5 \times 5 \times 5$ unit cell structure over a harmonic frequency sweep. The wave transmission curve along the excitation direction, measured in decibels (dB), was calculated as: $TL = 20\log_{10}\left(\frac{u_{out}}{u_{in}}\right)$, where $u_{out}$ is the output displacement at the center point of the top plate. These simulations provided theoretical transmission loss values for comparison with experimental results. For experimental validation, we conducted transmission loss measurements on both macroscale (10 mm SLA unit cell) and microscale (80 µm 2PP unit cell) samples. Each sample was excited from the bottom using piezo transducers, while the vibrational response across a frequency sweep was recorded at the top of the structure using a laser vibrometer. For the macroscale structure, transmission loss data were gathered over a frequency range of 1 to 90 kHz, while the microscale structure data were collected from 0.5 to 8 MHz. The vibrometer recorded velocity data, which were then processed using a FFT to obtain velocity magnitudes across frequencies. First, the piezo transducer's response was measured without any structure attached ($v_{piezo}$). Then, the measurements were repeated with the structures mounted on the transducer ($v_{structure}$). The velocity FFT was measured at the center of the top surface of the attached structure, and experimental transmission loss was calculated as: $TL = 20\log_{10}\left(\frac{v_{structure}}{v_{piezo}}\right)$.

Fig. 5 compares theoretical and experimental transmission loss diagrams for both the macroscale and microscale structures. Both structures exhibit distinct regions of reduced transmission corresponding to the predicted bandgap frequencies. The macroscale structure shows a significant drop in transmission within the bandgap range of 23–47 kHz, while the microscale structure exhibits similar behavior between 3.8–7.0 MHz. These results confirm the structures effectively block wave propagation within the desired frequency ranges, with the observed transmission loss peaks closely aligning with those predicted by simulations. The close agreement between the experimental and simulated results supports the robustness of the proposed design framework, though minor discrepancies were observed and attributed to fabrication tolerances, material variations, boundary effects, measurement noise and measurement error.

To further investigate these discrepancies, a quantitative error analysis was conducted using statistical metrics and additional simulations incorporating fabrication-induced variations. For the 80 µm 2PP structure (Fig. 5d), we observed a Median Absolute Error (MedAE) of 15 dB and a Pearson Correlation Coefficient of 0.786 between simulations and experiments, indicating a strong correlation despite expected deviations. Similarly, for the 10 mm SLA structure (Fig. 5a), we found a MedAE of 12.9 dB and a Pearson Correlation Coefficient of 0.64, further reinforcing the consistency between theoretical predictions and measured transmission loss. While minor variations exist, these results confirm that the overall bandgap characteristics remain largely

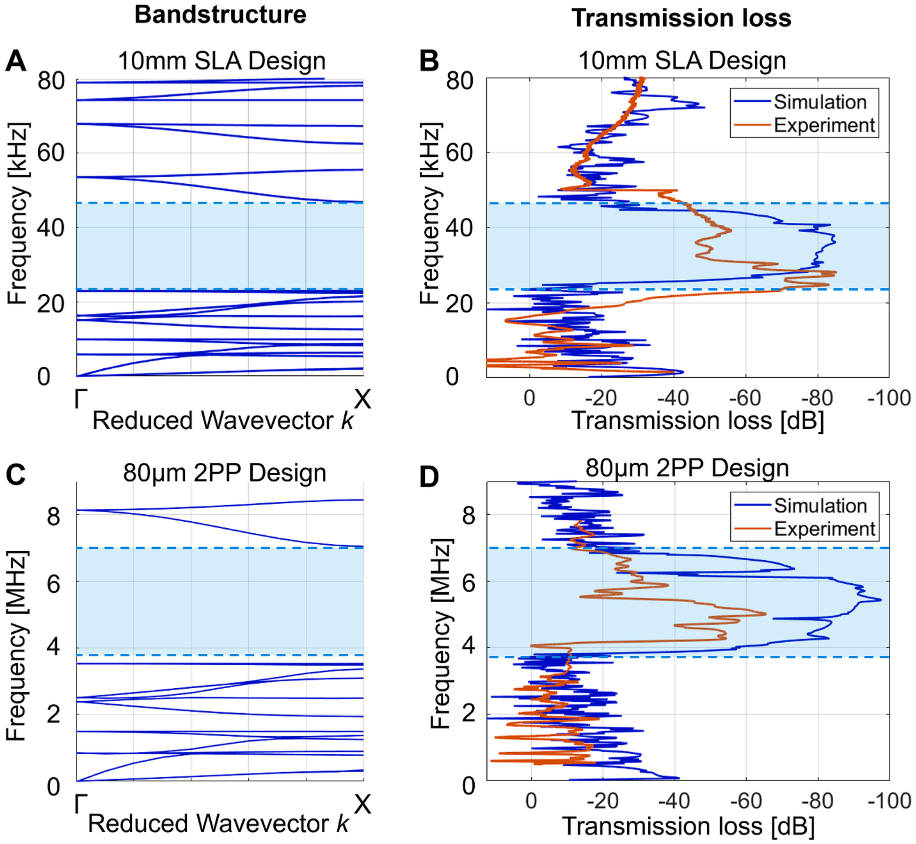

**Fig. 5. Comparison of theoretical and experimental transmission loss curves for phononic metamaterials at macro- and micro-scales.** A) Simulated band structure for waves propagating through the 10 mm unit cell fabricated using SLA. B) Transmission loss simulations (blue) and experimental measurements (red) for the 10 mm SLA structure. Both curves show significant attenuation within the bandgap range of 23–47 kHz, with close agreement between simulated and experimental results. C) Simulated band structure for waves propagating through the 80 µm unit cell fabricated using 2PP. D) Transmission loss simulations (blue) and experimental measurements (red) for the 80 µm 2PP structure. Both show strong attenuation within the bandgap frequency range of 3.8–7.0 MHz, with a high degree of alignment between theoretical predictions and measured results. For both structures, the regions of transmission loss match well with the predicted bandgaps, validating the modeling approach and confirming the ability of the structures to effectively block wave propagation within the anticipated frequency ranges.

preserved.

A primary source of deviation arises from fabrication imperfections, particularly in 2PP-fabricated microscale structures, where sub-micron to micron-scale geometric inaccuracies can influence the periodicity of the unit cell and alter resonance characteristics. To assess the impact of manufacturing-induced distortions, additional simulations were performed to evaluate Z-voxel elongation, a common artifact in 2PP printing. In these simulations, the originally spherical masses were modeled as ellipsoidal masses, where the major radius in the Z direction was increased by a factor of 1.5 while maintaining the unit cell volume fraction. The resulting modified bandgap range of 3.95–6.8 MHz closely aligned with both the original predicted range (3.8–7 MHz) and the experimental laser vibrometry measurements. The error metrics for these adjusted simulations yielded a MedAE of 11 dB and a Pearson Correlation Coefficient of 0.8, confirming that fabrication-induced geometric distortions play a significant role in shaping the experimental results. Despite these variations, the defect-adjusted simulations retained strong qualitative agreement with experimental transmission loss trends, reinforcing the predictive accuracy of the numerical modeling. These findings suggest that even with small manufacturing deviations, the overall phononic bandgap behavior remains robust, reinforcing the scalability of the proposed design framework.

Beyond systematic geometric distortions, localized defects were also considered. To evaluate their influence, we conducted additional simulations in which two random single beam elements were removed from the $5 \times 5 \times 5$ array to simulate a non-repeating structural defect, such as a broken beam. The results showed a high correlation coefficient (0.98) and a small median absolute deviation of 2 dB between the transmission loss curves of defected and non-defected structures. This suggests that while localized defects may cause minor wave propagation variations at specific locations, their overall impact on the bandgap characteristics is minimal when compared to systematic distortions. A detailed comparison of transmission loss across original simulations, experimental results, and defect-adjusted simulations is presented in SI Fig. S10.

Furthermore, variations in material properties influence the experimental results. Those disparities may stem from variations in the degree of polymerization [78]. The degree of conversion (DOC), which is influenced by the structuring laser intensity during fabrication, can significantly alter mechanical properties such as Young's modulus as well as optical characteristics. Lower DOCs may lead to incomplete polymerization, resulting in softer or less rigid structures that deviate from simulation assumptions. This phenomenon has been extensively reviewed in the literature [79] and can lead to shifts in the bandgap frequency range, as mechanical stiffness directly influences the propagation of elastic waves, as shown in SI Fig. S6.

In addition to fabrication and material variations, measurement uncertainties also contributed to the observed deviations. A key factor is the accuracy of laser vibrometry, particularly at high frequencies, where reduced signal-to-noise ratios can compromise measurement precision. Environmental fluctuations, including temperature and humidity variations, may also potentially affect bandgap behavior. Furthermore, solid-body motion artifacts, particularly in the microscale setup, can arise from the use of large piezo transducers, influencing the recorded transmission loss. While directly quantifying these effects remains challenging, experimental conditions were carefully controlled to minimize external influences. Additionally, FFT filtering was applied to mitigate low-frequency noise from external vibrations and environmental fluctuations, ensuring a more reliable analysis of transmission loss measurements.

Despite minor deviations attributed to the discussed factors, the overall agreement between simulated and experimental transmission loss data confirms the robustness of the proposed design framework. The combination of error analysis, defect-adjusted simulations, and material property assessments provides a comprehensive understanding of the sources of discrepancies, reinforcing the scalability and robustness of the designed geometries in achieving targeted bandgap performance. Future work should refine error quantification for environmental effects and boundary conditions to further enhance measurement reliability.

## 4. Discussion

This study introduces a scalable design framework for phononic bandgap metamaterials, offering an adaptable and practical approach to tuning bandgap properties through unit cell scaling. By focusing on the lattice constant as the primary parameter while allowing for secondary adjustments to strut and sphere dimensions, the framework simplifies the manipulation of bandgap properties and offers precise control over wave propagation.

Our framework enables highly tunable phononic bandgaps, achieving $B/\omega_c$ ratios up to 172 %, a level of tunability comparable to that achieved using highly complex unit cells and advanced optimization methods [13,29,48,55,56]. However, unlike other approaches, which often rely on computationally expensive topology optimization, genetic algorithms, or intricate resonator-based designs, our methodology remains intuitive, computationally lightweight, and easily scalable. By parameterizing the lattice constant as the primary tuning variable while allowing for controlled adjustments to strut and sphere dimensions, our framework provides a straightforward yet powerful means of tailoring bandgap properties across multiple frequency regimes.

A key component of our work is the experimental validation of bandgap tunability across multiple scales. While previous studies have primarily focused on either theoretical predictions or single-scale experimental validations, our approach bridges this gap by fabricating and testing optimized unit cells at both macroscale (10 mm, SLA) and microscale (80 μm, 2PP), confirming bandgap tunability across multiple orders of magnitude. The close agreement between experimental transmission loss measurements and theoretical simulations confirms the effectiveness of the design framework in guiding phononic metamaterial development.

While experimental and simulated transmission loss data showed strong agreement, minor discrepancies were identified, particularly at the microscale. As argued in the previous section, these deviations can be attributed to a combination of factors, including fabrication-induced distortions, material property variations, and measurement uncertainties. One of the primary sources of deviation stems from submicron to micron-scale geometric distortions inherent to 2PP fabrication. Defect-adjusted simulations incorporating these distortions yielded similar fit as experimental measurements to original simulation, underscoring that systematic fabrication artifacts significantly influence bandgap properties. These challenges are not unique and have been reported in previous studies [3,29,39,47,48], reinforcing the need for continuous improvement in fabrication techniques and measurement precision. Post-fabrication treatments like UV curing and heat treatment have been shown to enhance material uniformity and mechanical stability in similar 2PP applications [80,81], suggesting that such treatments could standardize Young's modulus across structures fabricated with different laser parameters, thus improving scalability and performance predictability.

Beyond fabrication-induced distortions, measurement uncertainties contributed to the observed deviations. Optical limitations of the laser vibrometer, particularly at higher frequencies, likely introduced background noise that affected measurement accuracy. Reduced signal-to-noise ratios at MHz frequencies in laser vibrometry can impact velocity measurements, making it challenging to resolve finer details of wave propagation. In addition, solid-body motion artifacts, particularly due to large piezo transducers in the microscale setup, contribute to experimental variability. These effects were mitigated through FFT filtering and controlled environmental conditions, yet further refinements in experimental setup could significantly improve measurement precision and reproducibility.

Despite these challenges, the overall strong agreement between experimental and theoretical results confirms the scalability and accuracy of the proposed design framework. As a control, an octet structure with comparable relative density and lattice constant to the original 10 mm unit cell was tested, and measurements (Fig. S9) confirmed the absence of a bandgap, as expected, further supporting the accuracy of the predicted bandgap behavior in our design and experimental framework.

Our framework's broad applicability and scalability stand out, offering a more computationally efficient alternative to conventional optimization methods. While emerging techniques such as machine learning-driven inverse design and multi-objective optimization offer promise for addressing nonlinear relationships between design parameters and bandgap properties, our parametric design framework provides a more accessible, intuitive, and effective tool for understanding how specific design choices influence bandgap characteristics. The colormaps presented in the study suggest new opportunities for advanced predictive modeling to complement the intuitive framework offered by the scaling law. Moreover, integrating material-specific speed-of-sound adjustments into the scaling law would improve its applicability across diverse materials and fabrication techniques, particularly given the distinct mechanical properties of microscale printing resins and macroscale materials. By leveraging 2PP's unparalleled precision and flexibility in fabrication of virtually any desired structural geometry, advanced predictive modeling can be directly translated into intricate physical designs, bridging the gap between theoretical predictions and experimental realizations.

## 5. Conclusion

This study presents a scalable and experimentally validated framework for designing phononic metamaterials with tunable bandgap properties across multiple length scales. By leveraging a parametrically controlled unit cell design, we demonstrated that bandgap characteristics can be systematically adjusted using a straightforward scaling law, enabling precise frequency tuning in both macroscale (SLA-fabricated) and microscale (2PP-fabricated) structures. Experimental validation confirmed the presence of bandgaps in the designed structures and their absence in control geometries, reinforcing the accuracy and robustness of our approach. While minor discrepancies between simulations and experiments were observed, these variations were within expected tolerances, primarily due to fabrication limitations, material property differences, and measurement constraints. The strong agreement between theoretical predictions and experimental results highlights the framework's reliability and adaptability. Beyond validating the scalability of phononic bandgap engineering, this research provides a foundation for future developments in metamaterial design. The framework offers a practical and computationally efficient methodology that can be extended to more complex unit cell geometries, alternative material systems, and diverse wave manipulation applications. With continued advancements in fabrication precision and computational modeling, this approach has the potential to accelerate the adoption of tunable phononic metamaterials in fields such as vibration isolation, waveguiding, and energy transfer, broadening their impact in engineering and applied physics.

## CRediT authorship contribution statement

**Timon Meier:** Writing – review & editing, Writing – original draft, Visualization, Validation, Software, Project administration, Methodology, Investigation, Formal analysis, Data curation, Conceptualization. **Vasileios Korakis:** Writing – review & editing, Writing – original draft, Methodology, Formal analysis, Data curation, Conceptualization. **Brian W. Blankenship:** Validation, Investigation, Data curation. **Haotian Lu:** Validation, Data curation. **Eudokia Kyriakou:** Validation, Data curation. **Savvas Papamakarios:** Validation, Data curation. **Zacharias Vangelatos:** Conceptualization. **M. Erden Yildizdag:** Conceptualization. **Gordon Zyla:** Validation, Data curation. **Xiaoxing Xia:** Validation, Data curation. **Xiaoyu Zheng:** Writing – review & editing. **Yoonsoo Rho:** Validation, Data curation. **Maria Farsari:** Writing – review & editing, Conceptualization. **Costas P. Grigoropoulos:** Writing – review & editing, Writing – original draft, Supervision, Project administration, Funding acquisition.

## Funding

We gratefully acknowledge funding support from multiple sources: the US National Science Foundation (grants 2134534 and 2124826), the Foundation for Education and European Culture (IPEP), and the European Union's Horizon Europe research and innovation program through a Marie Skłodowska-Curie Action (grant agreement No. 101059253). Additional support came from the joint funding initiative of the Stavros Niarchos Foundation (SNF) and the Hellenic Foundation for Research and Innovation (H.F.R.I.) under their 'Always Strive for Excellence – Theodore Papazoglou' program of the 'Science and Society' Action (Project Number: 9578). SEM images were obtained using Scios 2 DualBeam, available at the Biomolecular Nanotechnology Center of the California Institute for Quantitative Biosciences, UC Berkeley. 2PP fabrication was supported by Lawrence Livermore National Laboratory's Lab Directed Research and Development Program (23-ERD-027). Work at LLNL was performed under the auspices of the U.S. Department of Energy by Lawrence Livermore National Laboratory under Contract DE-AC52-07NA27344.

## Declaration of competing interest

The authors declare the following financial interests/personal relationships which may be considered as potential competing interests: Costas P. Grigoropoulos reports financial support was provided by National Science Foundation. Vasileios Korakis reports financial support was provided by Foundation for Education and European Culture. Gordon Zyla reports financial support was provided by Horizon Europe. Xiaoxing Xia reports financial support was provided by Lawrence Livermore National Laboratory. Xiaoxing Xia reports financial support was provided by US Department of Energy. Maria Farsari reports financial support was provided by Stavros Niarchos Foundation. Maria Farsari reports financial support was provided by Hellenic Foundation for Research and Innovation. If there are other authors, they declare that they have no known competing financial interests or personal relationships that could have appeared to influence the work reported in this paper.

## Appendix A. Supplementary data

Supplementary data to this article can be found online at https://doi.org/10.1016/j.matdes.2025.113778.

## Data availability

Supplementary material related to this article can be found online at the corresponding doi. The datasets and codes developed will be freely open sourced at the time of publication.

## References

[1] P.A. Deymier, ed., Acoustic Metamaterials and Phononic Crystals, Springer Berlin Heidelberg, Berlin, Heidelberg, 2013. 10.1007/978-3-642-31232-8.

[2] Z. Liu, X. Zhang, Y. Mao, Y.Y. Zhu, Z. Yang, C.T. Chan, P. Sheng, Locally resonant sonic materials, Science 289 (2000) 1734–1736, https://doi.org/10.1126/science.289.5485.1734.

[3] Y. Li, Y. Shen, S. Cao, X. Zhang, Y. Meng, Thermally triggered tunable vibration mitigation in Hoberman spherical lattice metamaterials, Appl. Phys. Lett. 114 (2019) 191904, https://doi.org/10.1063/1.5092423.

[4] S. Sepehri, H. Jafari, M.M. Mashhadi, M.R.H. Yazdi, M.M.S. Fakhrabadi, Study of tunable locally resonant metamaterials: effects of spider-web and snowflake

hierarchies, Int. J. Solids Struct. 204–205 (2020) 81–95, https://doi.org/10.1016/j.ijsolstr.2020.08.014.

[5] J.R. Raney, N. Nadkarni, C. Daraio, D.M. Kochmann, J.A. Lewis, K. Bertoldi, Stable propagation of mechanical signals in soft media using stored elastic energy, Proc. Natl. Acad. Sci. USA. 113 (2016) 9722–9727, https://doi.org/10.1073/pnas.1604838113.

[6] P. Delsing, A.N. Cleland, M.J.A. Schuetz, J. Knörzer, G. Giedke, J.I. Cirac, K. Srinivasan, M. Wu, K.C. Balram, C. Bäuerle, T. Meunier, C.J.B. Ford, P.V. Santos, E. Cerda-Méndez, H. Wang, H.J. Krenner, E.D.S. Nysten, M. Weiß, G.R. Nash, L. Thevenard, C. Gourdon, P. Rovillain, M. Marangolo, J.-Y. Duquesne, G. Fischerauer, W. Ruile, A. Reiner, B. Paschke, D. Denysenko, D. Volkmer, A. Wixforth, H. Bruus, M. Wiklund, J. Reboud, J.M. Cooper, Y. Fu, M.S. Brugger, F. Rehfeldt, C. Westerhausen, The 2019 surface acoustic waves roadmap, J. Phys. D: Appl. Phys. 52 (2019) 353001, https://doi.org/10.1088/1361-6463/ab1b04.

[7] H.-W. Dong, S.-D. Zhao, Y.-S. Wang, L. Cheng, C. Zhang, Robust 2D/3D multi-polar acoustic metamaterials with broadband double negativity, J. Mech. Phys. Solids 137 (2020) 103889, https://doi.org/10.1016/j.jmps.2020.103889.

[8] A.T. Fabro, D. Beli, N.S. Ferguson, J.R.F. Arruda, B.R. Mace, Wave and vibration analysis of elastic metamaterial and phononic crystal beams with slowly varying properties, Wave Motion 103 (2021) 102728, https://doi.org/10.1016/j.wavemoti.2021.102728.

[9] J. Li, X. Wu, C. Wang, Q. Huang, Sound insulation prediction and band gap characteristics of four vibrators acoustic metamaterial with composite phononic crystal structure, Mater. Today Commun. 37 (2023) 107455, https://doi.org/10.1016/j.mtcomm.2023.107455.

[10] M. Colletta, W. Gachuhi, S.A. Gartenstein, M.M. James, E.A. Szwed, B.C. Daly, W. Cui, G.A. Antonelli, Picosecond ultrasonic study of surface acoustic waves on periodically patterned layered nanostructures, Ultrasonics 87 (2018) 126–132, https://doi.org/10.1016/j.ultras.2018.02.013.

[11] L. Dhar, J.A. Rogers, High frequency one-dimensional phononic crystal characterized with a picosecond transient grating photoacoustic technique, Appl. Phys. Lett. 77 (2000) 1402–1404, https://doi.org/10.1063/1.1290388.

[12] J. Wang, F. Allein, N. Boechler, J. Friend, O. Vazquez-Mena, Design and fabrication of negative-refractive-index metamaterial unit cells for near-megahertz enhanced acoustic transmission in biomedical ultrasound applications, PhysRevApplied 15 (2021) 024025, https://doi.org/10.1103/PhysRevApplied.15.024025.

[13] C.W.L. Muhammad, Phononic metastructures with ultrawide low frequency three-dimensional bandgaps as broadband low frequency filter, Sci Rep 11 (2021) 7137, https://doi.org/10.1038/s41598-021-86520-8.

[14] W.P. Syam, W. Jianwei, B. Zhao, I. Maskery, W. Elmadih, R. Leach, Design and analysis of strut-based lattice structures for vibration isolation, Precis. Eng. 52 (2018) 494–506, https://doi.org/10.1016/j.precisioneng.2017.09.010.

[15] X. An, C. Lai, W. He, H. Fan, Three-dimensional meta-truss lattice composite structures with vibration isolation performance, Extreme Mech. Lett. 33 (2019) 100577, https://doi.org/10.1016/j.eml.2019.100577.

[16] J. Kim, H. Hegde, H. Kim, C. Lee, Spindle vibration mitigation utilizing additively manufactured auxetic materials, J. Manuf. Process. 73 (2022) 633–641, https://doi.org/10.1016/j.jmapro.2021.11.051.

[17] J. Boulvert, J. Costa-Baptista, T. Cavalieri, M. Perna, E.R. Fotsing, V. Romero-García, G. Gabard, A. Ross, J. Mardjono, J.-P. Groby, Acoustic modeling of micro-lattices obtained by additive manufacturing, Appl. Acoust. 164 (2020) 107244, https://doi.org/10.1016/j.apacoust.2020.107244.

[18] S. Cheng, J. Liang, Q. Ding, Q. Yan, Y. Sun, Y. Xin, L. Wang, Analysis of the band gap characteristics of a new type of three-dimensional single phase phononic crystal, Wave Motion 122 (2023) 103195, https://doi.org/10.1016/j.wavemoti.2023.103195.

[19] C. Claeys, N.G. Rocha De Melo Filho, L. Van Belle, E. Deckers, W. Desmet, Design and validation of metamaterials for multiple structural stop bands in waveguides, Extreme Mechanics Letters 12 (2017) 7–22. 10.1016/j.eml.2016.08.005.

[20] Y. Chen, T. Li, F. Scarpa, L. Wang, Lattice metamaterials with mechanically tunable Poisson's ratio for vibration control, PhysRevApplied 7 (2017) 024012, https://doi.org/10.1103/PhysRevApplied.7.024012.

[21] Y. Li, E. Baker, T. Reissman, C. Sun, W.K. Liu, Design of mechanical metamaterials for simultaneous vibration isolation and energy harvesting, Appl. Phys. Lett. 111 (2017) 251903, https://doi.org/10.1063/1.5008674.

[22] B. Wang, C. Xu, G. Duan, W. Xu, F. Pi, Review of broadband metamaterial absorbers: from principles design strategies, and tunable properties to functional applications, Adv. Funct. Mater. 33 (2023) 2213818, https://doi.org/10.1002/adfm.202213818.

[23] M. Bakaric, P. Miloro, A. Javaherian, B.T. Cox, B.E. Treeby, M.D. Brown, Measurement of the ultrasound attenuation and dispersion in 3D-printed photopolymer materials from 1 to 3.5 MHz, The Journal of the Acoustical Society of America 150 (2021) 2798–2805, https://doi.org/10.1121/10.0006668.

[24] M.S. Kushwaha, P. Halevi, L. Dobrzynski, B. Djafari-Rouhani, Acoustic band structure of periodic elastic composites, PhysRevLett.7 71 (1993) 2022–2025, https://doi.org/10.1103/PhysRevLett.71.2022.

[25] M. Cenedese, E. Belloni, F. Braghin, Interaction of Bragg scattering bandgaps and local resonators in mono-coupled periodic structures, J. Appl. Phys. 129 (2021) 124501, https://doi.org/10.1063/5.0038438.

[26] I.V. Andrianov, V.V. Danishevskyy, G. Rogerson, Elastic waves in periodically heterogeneous two-dimensional media: locally periodic and anti-periodic modes, Proc. R. Soc. A. 474 (2018) 20170908, https://doi.org/10.1098/rspa.2017.0908.

[27] M.H. Bae, J.H. Oh, Amplitude-induced bandgap: New type of bandgap for nonlinear elastic metamaterials, J. Mech. Phys. Solids 139 (2020) 103930, https://doi.org/10.1016/j.jmps.2020.103930.

[28] E. Turco, E. Barchiesi, F. dell'Isola, A numerical investigation on impulse-induced nonlinear longitudinal waves in pantographic beams, Math. Mech. Solids 27 (2022) 22–48, https://doi.org/10.1177/10812865211010877.

[29] Y. Li, S. Cao, Y. Shen, Y. Meng, Phononic band-gaps of Hoberman spherical metamaterials in low frequencies, Mater. Des. 181 (2019) 107935, https://doi.org/10.1016/j.matdes.2019.107935.

[30] R. Martínez-Sala, J. Sancho, J.V. Sánchez, V. Gómez, J. Llinares, F. Meseguer, Sound attenuation by sculpture, Nature 378 (1995) 241, https://doi.org/10.1038/378241a0.

[31] A.O. Krushynska, P. Galich, F. Bosia, N.M. Pugno, S. Rudykh, Hybrid metamaterials combining pentamode lattices and phononic plates, Appl. Phys. Lett. 113 (2018) 201901, https://doi.org/10.1063/1.5052161.

[32] K.K. Dudek, J.A.I. Martínez, G. Ulliac, L. Hirsinger, L. Wang, V. Laude, M. Kadic, Micro-scale mechanical metamaterial with a controllable transition in the Poisson's ratio and band gap formation, Adv. Mater. 35 (2023) 2210993, https://doi.org/10.1002/adma.202210993.

[33] K.K. Dudek, L. Mizzi, J.A. Iglesias Martínez, A. Spaggiari, G. Ulliac, R. Gatt, J. N. Grima, V. Laude, M. Kadic, Micro-scale graded mechanical metamaterials exhibiting versatile Poisson's ratio, Composite Structures 319 (2023) 117151, https://doi.org/10.1016/j.compstruct.2023.117151.

[34] D. Mousanezhad, B. Haghpanah, R. Ghosh, A.M. Hamouda, H. Nayeb-Hashemi, A. Vaziri, Elastic properties of chiral, anti-chiral, and hierarchical honeycombs: a simple energy-based approach, Theor. Appl. Mech. Lett. 6 (2016) 81–96, https://doi.org/10.1016/j.taml.2016.02.004.

[35] L. Placidi, G. Rosi, I. Giorgio, A. Madeo, Reflection and transmission of plane waves at surfaces carrying material properties and embedded in second-gradient materials, Math. Mech. Solids 19 (2014) 555–578, https://doi.org/10.1177/1081286512474016.

[36] Y. Xie, Y. Fu, Z. Jia, J. Li, C. Shen, Y. Xu, H. Chen, S.A. Cummer, Acoustic imaging with metamaterial luneburg lenses, Sci. Rep. 8 (2018) 16188, https://doi.org/10.1038/s41598-018-34581-7.

[37] L. Shao, D. Zhu, M. Colangelo, D. Lee, N. Sinclair, Y. Hu, P.T. Rakich, K. Lai, K. K. Berggren, M. Lončar, Electrical control of surface acoustic waves, Nat. Electron 5 (2022) 348–355, https://doi.org/10.1038/s41928-022-00773-3.

[38] J. Ma, Phonon engineering of micro- and nanophononic crystals and acoustic metamaterials: a review, Small Sci. 3 (2023) 2200052, https://doi.org/10.1002/smsc.202200052.

[39] M.F. Groß, J.L.G. Schneider, Y. Wei, Y. Chen, S. Kalt, M. Kadic, X. Liu, G. Hu, M. Wegener, Tetramode metamaterials as phonon polarizers, Adv. Mater. 35 (2023) 2211801, https://doi.org/10.1002/adma.202211801.

[40] G. Zyla, M. Farsari, Frontiers of laser-based 3D printing: a perspective on multi-photon lithography, Laser & Photonics Reviews 18 (2024) 2301312, https://doi.org/10.1002/lpor.202301312.

[41] S. Papamakarios, O. Tsilipakos, I. Katsantonis, A.D. Koulouklidis, M. Manousidaki, G. Zyla, C. Daskalaki, S. Tzortzakis, M. Kafesaki, M. Farsari, Cactus-like metamaterial structures for electromagnetically induced transparency at THz FREQUENCIES, ACS Photonics (2024) acsphotonics.4c01179, https://doi.org/10.1021/acsphotonics.4c01179.

[42] G. Zyla, G. Maconi, A. Nolvi, J. Marx, D. Ladika, A. Salmi, V. Melissinaki, I. Kassamakov, M. Farsari, 3D micro-devices for enhancing the lateral resolution in optical microscopy, Gxjzz 5 1 (2024) 10.37188/lam.2024.019.

[43] R. Sun, J. Lem, Y. Kai, W. DeLima, C.M. Portela, Tailored ultrasound propagation in microscale metamaterials via inertia design, Sci. Adv. 10 (2024) eadq6425, https://doi.org/10.1126/sciadv.adq6425.

[44] Y. Kai, S. Dhulipala, R. Sun, J. Lem, W. DeLima, T. Pezeril, C.M. Portela, Dynamic diagnosis of metamaterials through laser-induced vibrational signatures, Nature 623 (2023) 514–521, https://doi.org/10.1038/s41586-023-06652-x.

[45] B. Telgen, V. Kannan, J.-C. Bail, C. Dorn, H. Niese, D.M. Kochmann, Rainbow trapping of out-of-plane mechanical waves in spatially variant beam lattices, J. Mech. Phys. Solids 191 (2024) 105762, https://doi.org/10.1016/j.jmps.2024.105762.

[46] R. Tang, T. Lu, C. Pan, W. Zheng, Vibrational loss analysis of a new type of phononic crystal with a tungsten block embedded inside a rubber matrix, Journal of Low Frequency Noise, Vibration and Active Control 42 (2023) 1765–1774, https://doi.org/10.1177/14613484231185473.

[47] N. Aravantinos-Zafiris, F. Lucklum, M.M. Sigalas, Complete phononic band gaps in the 3D Yablonovite structure with spheres, Ultrasonics 110 (2021) 106265, https://doi.org/10.1016/j.ultras.2020.106265.

[48] J.A. Iglesias Martínez, J. Moughames, G. Ulliac, M. Kadic, V. Laude, Three-dimensional phononic crystal with ultra-wide bandgap at megahertz frequencies, Appl. Phys. Lett. 118 (2021) 063507, https://doi.org/10.1063/5.0033615.

[49] Z. Jia, Y. Chen, H. Yang, L. Wang, Designing phononic crystals with wide and robust band gaps, PhysRevApplied 9 (2018) 044021, https://doi.org/10.1103/PhysRevApplied.9.044021.

[50] R.H. Olsson Iii, I. El-Kady, Microfabricated phononic crystal devices and applications, Meas. Sci. Technol. 20 (2009) 012002, https://doi.org/10.1088/0957-0233/20/1/012002.

[51] C. Goffaux, J.P. Vigneron, Theoretical study of a tunable phononic band gap system, PhysRevB 64 (2001) 075118, https://doi.org/10.1103/PhysRevB.64.075118.

[52] Z. Tao, X. Ren, A.G. Zhao, L. Sun, Y. Zhang, W. Jiang, D. Han, X.Y. Zhang, Y.M. Xie, A novel auxetic acoustic metamaterial plate with tunable bandgap, Int. J. Mech. Sci. 226 (2022) 107414, https://doi.org/10.1016/j.ijmecsci.2022.107414.

[53] S. Ning, F. Yang, C. Luo, Z. Liu, Z. Zhuang, Low-frequency tunable locally resonant band gaps in acoustic metamaterials through large deformation, Extreme Mech. Lett. 35 (2020) 100623, https://doi.org/10.1016/j.eml.2019.100623.

[54] K. Zhang, P. Zhao, C. Zhao, F. Hong, Z. Deng, Study on the mechanism of band gap and directional wave propagation of the auxetic chiral lattices, Compos. Struct. 238 (2020) 111952, https://doi.org/10.1016/j.compstruct.2020.111952.

[55] H. Ronellenfitsch, N. Stoop, J. Yu, A. Forrow, J. Dunkel, Inverse design of discrete mechanical metamaterials, PhysRevMaterials 3 (2019) 095201, https://doi.org/10.1103/PhysRevMaterials.3.095201.

[56] X. Zhang, H. Ye, N. Wei, R. Tao, Z. Luo, Design optimization of multifunctional metamaterials with tunable thermal expansion and phononic bandgap, Mater. Des. 209 (2021) 109990, https://doi.org/10.1016/j.matdes.2021.109990.

[57] B. Fang, R. Zhang, T. Chen, W. Wang, J. Zhu, W. Cheng, Bandgap optimization and inverse design of labyrinth metamaterials for sound insulation, Journal of Building Engineering 86 (2024) 108898, https://doi.org/10.1016/j.jobe.2024.108898.

[58] O. Sigmund, J. Søndergaard Jensen, Systematic design of phononic band–gap materials and structures by topology optimization, Philosophical Transactions of the Royal Society of London Series A: Mathematical, Physical and Engineering Sciences 361 (2003) 1001–1019, https://doi.org/10.1098/rsta.2003.1177.

[59] A. Dalklint, M. Wallin, K. Bertoldi, D. Tortorelli, Tunable phononic bandgap materials designed via topology optimization, J. Mech. Phys. Solids 163 (2022) 104849, https://doi.org/10.1016/j.jmps.2022.104849.

[60] Y. Li, G. Yin, G. Yan, S. Yao, Forward-backstepping design of phononic crystals with anticipated band gap by data-driven method, Mech. Syst. Sig. Process. 224 (2025) 111975, https://doi.org/10.1016/j.ymssp.2024.111975.

[61] Y. Jin, L. He, Z. Wen, B. Mortazavi, H. Guo, D. Torrent, B. Djafari-Rouhani, T. Rabczuk, X. Zhuang, Y. Li, Intelligent on-demand design of phononic metamaterials, Nanophotonics 11 (2022) 439–460, https://doi.org/10.1515/nanoph-2021-0639.

[62] D. Lee, B.D. Youn, S.-H. Jo, Deep-learning-based framework for inverse design of a defective phononic crystal for narrowband filtering, Int. J. Mech. Sci. 255 (2023) 108474, https://doi.org/10.1016/j.ijmecsci.2023.108474.

[63] M. Maurizi, D. Xu, Y.-T. Wang, D. Yao, D. Hahn, M. Oudich, A. Satpati, M. Bauchy, W. Wang, Y. Sun, Y. Jing, X.R. Zheng, Inverse designing metamaterials with programmable nonlinear functional responses in graph space, (2024). 10.48550/ARXIV.2408.06300.

[64] E. Yablonovitch, T. Gmitter, K. Leung, Photonic band structure: The face-centered-cubic case employing nonspherical atoms, PhysRevLett. 67 (1991) 2295–2298, https://doi.org/10.1103/PhysRevLett.67.2295.

[65] T. Gorishnyy, C.K. Ullal, M. Maldovan, G. Fytas, E.L. Thomas, Hypersonic phononic crystals, PhysRevLett. 94 (2005) 115501, https://doi.org/10.1103/PhysRevLett.94.115501.

[66] L. D'Alessandro, E. Belloni, R. Ardito, A. Corigliano, F. Braghin, Modeling and experimental verification of an ultra-wide bandgap in 3D phononic crystal, Appl. Phys. Lett. 109 (2016) 221907, https://doi.org/10.1063/1.4971290.

[67] T. Meier, R. Li, S. Mavrikos, B. Blankenship, Z. Vangelatos, M.E. Yildizdag, C. P. Grigoropoulos, Obtaining auxetic and isotropic metamaterials in counterintuitive design spaces: an automated optimization approach and experimental characterization, Npj Comput Mater 10 (2024) 3, https://doi.org/10.1038/s41524-023-01186-2.

[68] H.M. Sheikh, T. Meier, B. Blankenship, Z. Vangelatos, N. Zhao, P.S. Marcus, C. P. Grigoropoulos, Systematic design of Cauchy symmetric structures through Bayesian optimization, Int. J. Mech. Sci. 236 (2022) 107741, https://doi.org/10.1016/j.ijmecsci.2022.107741.

[69] C. Dorn, D.M. Kochmann, Ray theory for elastic wave propagation in graded metamaterials, J. Mech. Phys. Solids 168 (2022) 105049, https://doi.org/10.1016/j.jmps.2022.105049.

[70] W. Setyawan, S. Curtarolo, High-throughput electronic band structure calculations: challenges and tools, Comput. Mater. Sci 49 (2010) 299–312, https://doi.org/10.1016/j.commatsci.2010.05.010.

[71] W. Elmadih, D. Chronopoulos, J. Zhu, Metamaterials for simultaneous acoustic and elastic bandgaps, Sci. Rep. 11 (2021) 14635, https://doi.org/10.1038/s41598-021-94053-3.

[72] C. Kittel, Introduction to solid state physics, Global edition, [9th edition], Wiley, Hoboken, NJ, 2018.

[73] R.S. Langley, The response of two-dimensional periodic structures to point harmonic forcing, J. Sound Vib. 197 (1996) 447–469, https://doi.org/10.1006/jsvi.1996.0542.

[74] D.J. Colquitt, V.V. Danishevskyy, J. Kaplunov, Composite dynamic models for periodically heterogeneous media, Math. Mech. Solids 24 (2019) 2663–2693, https://doi.org/10.1177/1081286518776704.

[75] M.M. Sigalas, E.N. Economou, Elastic and acoustic wave band structure, J. Sound Vib. 158 (1992) 377–382, https://doi.org/10.1016/0022-460X(92)90059-7.

[76] A.R.H. Alhawari, T. Saeidi, A.H.M. Almawgani, A.T. Hindi, H. Alghamdi, T. Alsuwian, S.A.B. Awwad, M.A. Imran, Wearable metamaterial dual-polarized high isolation UWB MIMO vivaldi antenna for 5G and satellite communications, Micromachines 12 (2021) 1559, https://doi.org/10.3390/mi12121559.

[77] B. Li, Y. Ding, D.Y. Kim, L. Wang, T.-C. Weng, W. Yang, Z. Yu, C. Ji, J. Wang, J. Shu, J. Chen, K. Yang, Y. Xiao, P. Chow, G. Shen, W.L. Mao, H.-K. Mao, Probing the electronic band gap of solid hydrogen by inelastic X-ray scattering up to 90 GPa, PhysRevLett. 126 (2021) 036402, https://doi.org/10.1103/PhysRevLett.126.036402.

[78] J. Bauer, A. Guell Izard, Y. Zhang, T. Baldacchini, L. Valdevit, Programmable mechanical properties of two-photon polymerized materials: from nanowires to bulk, Adv. Mater. Tech. 4 (2019) 1900146, https://doi.org/10.1002/admt.201900146.

[79] H. Wang, W. Zhang, D. Ladika, H. Yu, D. Gailevičius, H. Wang, C. Pan, P.N.S. Nair, Y. Ke, T. Mori, J.Y.E. Chan, Q. Ruan, M. Farsari, M. Malinauskas, S. Juodkazis, M. Gu, J.K.W. Yang, Two-photon polymerization lithography for optics and photonics: fundamentals materials, technologies, and applications, Adv. Funct. Mater. 33 (2023) 2214211, https://doi.org/10.1002/adfm.202214211.

[80] M. Schmid, D. Ludescher, H. Giessen, Optical properties of photoresists for femtosecond 3D printing: refractive index, extinction, luminescence-dose dependence, aging, heat treatment and comparison between 1-photon and 2-photon exposure, Opt. Mater. Express 9 (2019) 4564, https://doi.org/10.1364/OME.9.004564.

[81] G. Merkininkaitė, E. Aleksandravičius, M. Malinauskas, D. Gailevičius, S. Šakirzanovas, Faculty of Chemistry and Geosciences, Vilnius University, Naugarduko Str. 24, Vilnius LT-03225, Lithuania, Femtika, Sauletekio Ave. 15, Vilnius LT-10224, Lithuania, Laser Research Center, Physics Faculty, Vilnius University, Sauletekio Ave. 10, Vilnius LT-10223, Lithuania, Department of Chemical Engineering and Technology, Center for Physical Sciences and Technology, Sauletekio Ave. 3, Vilnius LT-10257, Lithuania, Laser additive manufacturing of Si/$ZrO_2$ tunable crystalline phase 3D nanostructures, OEA 5 (2022) 210077–210077. 10.29026/oea.2022.210077.